Marine Pollution Bulletin 227 (2026) 119450

Contents lists available at ScienceDirect

Marine Pollution Bulletin

journal homepage: www.elsevier.com/locate/marpolbul

Assessing the impacts of offshore wind turbines on suspended sediments concentration in northern China coastal waters on the basis of Sentinel-1/2

Yingzhuo Hou [a,b], Dingfeng Yu [c], Qianguo Xing [a,b,*], Shanshan Jiang [a,b], Rongda Guan [a,b], Maham Arif [a,b], Xiangyang Zheng [a,b], Jianmin Zhao [a,b]

[a] Shandong Key Laboratory of Coastal Zone Environmental Processes and Ecological Security, Yantai Institute of Coastal Zone Research, Chinese Academy of Sciences, Yantai, 264003, China
[b] University of Chinese Academy of Sciences, Beijing, 100049, China
[c] Institute of Oceanographic Instrumentation, Qilu University of Technology (Shandong Academy of Sciences), Qingdao, 266061, China

ARTICLE INFO

Keywords:
Offshore wind turbine
Wind turbine water surface wake
Suspended sediment concentration
Sentinel-1/2
The Bohai Sea
The Yellow Sea

ABSTRACT

The disturbance by offshore wind turbines on water, brings strong vertical mixing of substances in the water, which not only impacts the aquatic ecosystem but also threatens the stability of pile foundations for offshore wind turbines. The suspended sediment concentration (SSC) serves as a reliable index for monitoring the effects of wind turbines on water mass. This study utilizes Sentinel-1 SAR satellite images to identify offshore wind turbines and to monitor the evolution of wind farms in northern China coastal waters, while Sentinel-2 optical satellite is used to monitor the Scaled Index of Suspended Sediments Wake (SI-SSW) caused by wind turbines. The results derived from Sentinel-1 images show that the total area of offshore wind farms increased to about 6300 km^2 by 15 times over the past decade, with an increase in the total number of offshore wind turbines from 322 in 2016 to 3840 in 2024 and an expansion in distribution towards deep sea. The results from Sentinel-2 optical imagery show that the affected area by one single wind turbine indicated by the SSC and the SI-SSW ranged from 0.3 km^2 to 1.5 km^2, which means about 5800 km^2 of water was affected by wind farms in the northern China coastal waters. The SSC, due to resuspension, could be elevated by more than 20% in the wind turbine wakes. In this work, the effects of tidal patterns, water depth, and the volume of the turbine's foundation on the wakes are also explored. The proposed methods and the findings would provide supports on assessing the impacts of offshore wind farms and the related decision-making.

1. Introduction

In recent years, the rapid development of clean energy facilities–including solar, wind, and tidal energy–has been driven by the urgent need to mitigate global warming (Cui et al., 2021; Dincer and Acar, 2015; IEA, 2024). As a major maritime nation, China possesses abundant offshore wind energy resources (Zheng and Li, 2023) and leads globally in offshore wind power construction (CREIA, 2023). China's offshore wind power industry has progressed through three distinct development phases (Liu, 2024): the initial stage (2007–2010), marked by technological exploration and the testing and demonstration of wind power projects; the slow development stage (2010–2015), characterized by the completion of demonstration wind farms and the accumulation of experience; and the rapid development stage (2015–present), driven by policy support, industry standardization, and large-scale wind farm construction. In 2023, the proportion of offshore wind turbines with a unit capacity of 10 MW and above increased significantly from 12.1% in 2022 to 46.4% (CREIA, 2024). Additionally, the maximum capacity of newly installed (the latest installation of that year) single turbines rose from 11 MW to 16.5 MW. By 2024, China's newly installed offshore wind power capacity was 4.04 GW, contributing to a cumulative grid-connected capacity of 41.27 GW (National Energy Administration, 2025). The Bohai Sea and Yellow Sea are critical regions for the development of offshore wind farms in China, due to their abundant wind energy resources and suitable water depths (Jiang et al., 2023; Zhang and Wang, 2022). In recent years, driven by policy support and growing energy demand, the construction of offshore wind turbines in both areas has rapidly expanded (Fu and Zhang, 2024; Jiang, 2022). While the

* Corresponding author at: Shandong Key Laboratory of Coastal Zone Environmental Processes and Ecological Security, Yantai Institute of Coastal Zone Research, Chinese Academy of Sciences, Yantai, 264003, China.
E-mail address: qgxing@yic.ac.cn (Q. Xing).

https://doi.org/10.1016/j.marpolbul.2026.119450
Received 20 August 2025; Received in revised form 15 February 2026; Accepted 18 February 2026

increasing offshore wind farms provide more clean energy, the associated environmental impacts cannot be overlooked (Hernandez et al., 2021; Su et al., 2020; Xu et al., 2015).

The impacts of offshore wind turbines on the marine environment are primarily in the construction and operation phases (Wang et al., 2022; Xu et al., 2015). During construction, pile foundation installation and cable laying disrupt benthic habitats, causing the death of some benthic organisms and promoting seabed sediment resuspension (Feng et al., 2023; Langhamer et al., 2018). During the operational phase, offshore wind turbines affect bird migration and alter the visual and auditory perception of surrounding marine organisms (Mendel et al., 2019; Spiga et al., 2017; Vanermen et al., 2015). Wake vortices generated near the pile foundations of wind turbines lead to sediment resuspension and redistribution (Bailey et al., 2024; Vanhellemont and Ruddick, 2014; Wang et al., 2023), which can erode the tower foundation and pose safety risks to the wind turbine. In addition, sediment resuspension trails at the sea surface affect the optical properties and ecological environment of the water bodies. Suspended sediment concentration (SSC) is a crucial water quality indicator. Analyzing the impacts of offshore wind turbines on SSC is essential for water quality management and comprehensive environmental assessment.

Precise localization of offshore wind turbines is critical for assessing their impacts on the marine environment. Extensive research has been conducted on the remote sensing monitoring of offshore wind turbines, employing multispectral and microwave imagery (Wong et al., 2019; Xu et al., 2020; Zhang et al., 2021; Hoeser et al., 2022). Notably, microwave imagery offers a distinct advantage due to its insensitivity to atmospheric cloud cover, making it particularly effective for observing artificial offshore structures. The investigation of SSC in water bodies is primarily conducted through two methods: traditional field surveys and remote sensing monitoring. In comparison to traditional methods, satellite remote sensing provides advantages such as extensive spatial coverage, continuous temporal observation, and reduced costs, establishing it as an indispensable tool for monitoring marine water quality (Chu et al., 2022; Xing et al., 2013). Currently, numerous studies on remote sensing methods for monitoring SSC have established a mature system, encompassing empirical, semi-analytical, and analytical models (Bernardo et al., 2019; Han et al., 2016; Liu et al., 2021). In addition, with the advancements in artificial intelligence, methods such as neural networks, machine learning, and deep learning have been extensively applied to monitor SSC (Fang et al., 2019; Jiang et al., 2021; Xie et al., 2024). However, these methods require extensive field data input and often provide relatively weaker explanations of physical mechanisms (Yang et al., 2022). Empirical models are particularly favored for their simplicity and minimal parameter requirements, making them widely adopted by researchers (Chen et al., 2022; He et al., 2013).

To assess the impacts of artificial structures such as offshore wind turbines and offshore platforms on SSC, researchers typically rely on field measurements or numerical simulation data (Baeye and Fettweis, 2015; Bailey et al., 2024; Hendriks et al., 2025; Kuang et al., 2014; Wang et al., 2021; Zhou et al., 2023). However, these analyses are often limited in scope, and the accuracy of numerical models requires further evaluation. Satellite remote sensing technology provides a direct reflection of water quality around offshore wind turbines, enabling large-scale continuous observation. It is a crucial method for monitoring the wake of offshore wind turbines and the SSC in the surrounding water bodies. Li et al. (2014) identified surface wakes in synthetic aperture radar (SAR) imagery, attributed to tidal currents interacting with offshore wind turbine structures. Vanhellemont and Ruddick (2014) utilized Landsat 8 imagery to monitor SSC in offshore wind farm areas, measuring the length of the surface wakes behind wind turbines and observing elevated SSC within these wake regions. Brandao et al. (2023) analyzed the temporal and spatial variations in SSC in the northern Dutch seas before and after wind turbine construction using Landsat composite imagery, finding that the impact of wind turbine construction on SSC was not significant. This result differed from their expectations, likely due to the considerable distance between the wind farm and the reference area, the influence of varying environmental conditions, and the low spatial resolution of the imagery used in the analysis. Cai et al. (2023) analyzed the impact of offshore wind turbines on SSC in the Yangtze River estuary using GF 6 (Gaofen 6) imagery and found that SSC within the wind farm was significantly higher than in the surrounding waters. Lecordier et al. (2025) directly analyzed the SSC in the wakes of offshore wind turbines in the southern North Sea using Sentinel-2 and Landsat-8/9 imagery and found that the downstream SSC was consistently higher than upstream across seasons, with sediment wake intensity influenced by factors such as pile foundation size, shape, water depth, wind, and hydrodynamic conditions. Building on their approach, the suspended sediment wake was analyzed within a 100–350 m fan-shaped surface buffer, a constraint that may have led to partial omission of wake signals and inadvertent inclusion of background seawater, thereby introducing additional uncertainty into the wake estimation.

Previous studies investigating the impacts of wind turbines on water SSC using satellite imagery have primarily focused on the SSC differences between wind farms and surrounding waters. However, this approach may introduce assessment errors due to variations in natural environmental factors. Direct assessments of SSC in the wind turbine wakes remain limited and warrant further investigation. The low spatial resolution of previous imagery likely limited the analyses of SSC in the wind turbine wakes. Sentinel-2 imagery with a 10-m spatial resolution allows for more precise monitoring of SSC in these wakes. This study aims to extract and analyze the evolution of offshore wind turbines in northern China coastal waters using Sentinel-1 microwave imagery, and to extract the water surface wakes of the wind turbines and quantify the SSC of individual wakes using high spatial resolution Sentinel-2 multispectral imagery and empirical models, thereby assessing the influence of offshore wind turbines on SSC. The findings provide valuable insights for the planning and environmental management of offshore wind turbines.

2. Data and methods

2.1. Study area

The study area is located in northern China coastal waters (the Bohai Sea and the Yellow Sea), as shown in Fig. 1. The Bohai Sea has a long history of wind energy development, with China's first offshore wind turbine installed in Bohai Bay in 2007 (Qin, 2022). The northernmost wind farm in the Bohai Sea is located in Caofeidian, between Caofeidian Port and Jingtang Port, and is the country's first cold-resistant offshore wind farm (Fan et al., 2018; Zhao et al., 2022). On October 17, 2016, the first large-scale single offshore wind farm was constructed in China, located in Jiangsu (Jiang, 2016). The analysis of the impact of wind turbines on SSC in the marine environment is exemplified by wind farms in southern Bohai Bay, approximately 12 km from Dongying Port (Fig. 1 (g)) and Yancheng City in Jiangsu Province (Fig. 1(c)).

2.2. Datasets

The satellite data in this study include Sentinel-1 VV polarization imagery and Sentinel-2 multispectral imagery. Sentinel-1 images were accessed via the Google Earth Engine (GEE) platform and were utilized for extracting offshore wind turbines. The time range of the images spans from October 1 to December 31 annually, between 2016 and 2024. Sentinel-2 imagery data were downloaded from the Copernicus Data Space Ecosystem official website (https://dataspace.copernicus.eu/), with spatial resolutions of 10 m and 20 m for the selected image bands. For the extraction of wake patterns and monitoring of SSC at offshore wind turbines in the Bohai Bay and Jiangsu, Sentinel-2 imagery from August 14, 2023, and May 23, 2023, was used as examples. In the discussion section, the analysis of wake characteristics of offshore wind turbines is based on Sentinel-2 imagery from the Bohai Bay in 2023. In

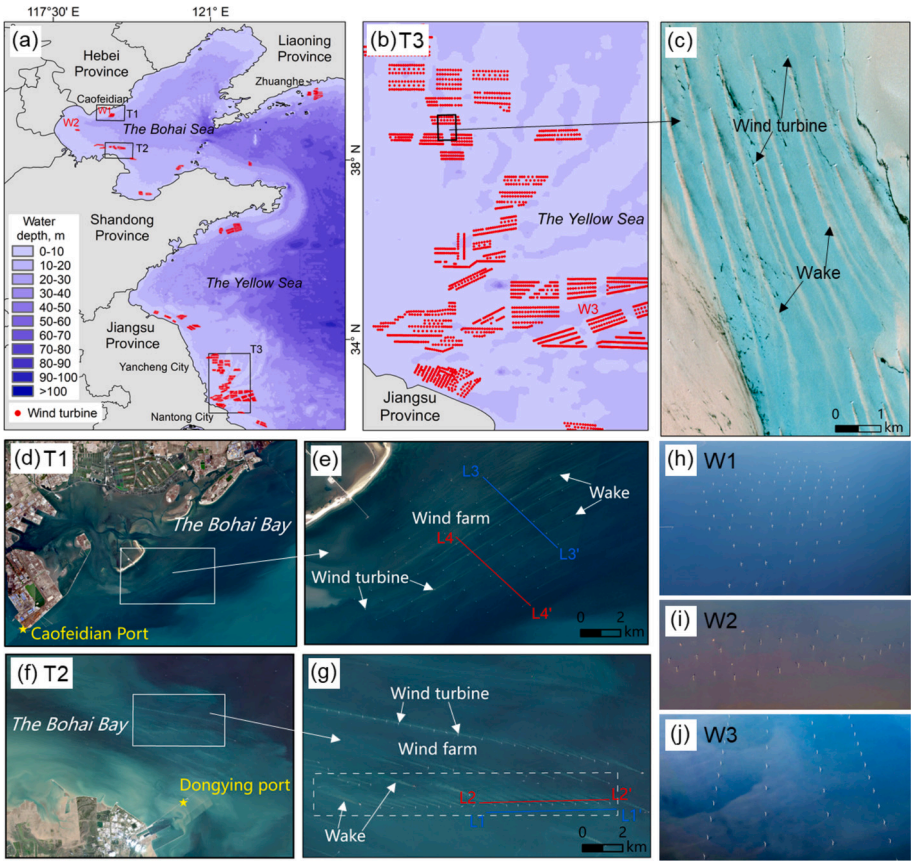

Fig. 1. (a) Distribution of offshore wind turbines in northern China coastal waters in 2024. (b) A zoomed-in view of the black box near Yancheng City (box T3 in (a)). (c) True-color Sentinel-2 image dated May 23, 2023, within the black box in (b). (d) and (f) true-color Sentinel-2 images from March 30, 2023, and August 14, 2023, respectively, showing the black boxes near Caofeidian (box T1 in (a)) and the southern Bohai Bay (box T2 in (a)). (e) and (g) zoomed-in views of the white boxes in (d) and (f), respectively. Profiles are indicated in (e) and (g), such as profile L1-L1′. (h), (i) and (j) aerial photos of wind farms in the Caofeidian (W1, captured on March 5, 2024), the western Bohai Bay (W2, captured on January 8, 2025) and the Jiangsu shoal (W3, captured on September 9, 2023), respectively.

the southern nearshore wind farm area of Bohai Bay, a total of 35 images were selected; for the offshore wind farm area of Caofeidian, 46 images were selected. All Sentinel-2 satellite imagery used in this study consists of Level-2A products, which have undergone both atmospheric and geometric corrections. Additionally, auxiliary data such as tidal data were obtained from the National Marine Data Center (NMDC) website (https://mds.nmdis.org.cn/pages/tidalCurrent.html), and bathymetric data were sourced from the General Bathymetric Chart of the Oceans (GEBCO) website (https://www.gebco.net/). Surface current velocity data for nearby stations used in this study were sourced from the Global Ocean Physics Analysis and Forecast dataset, available for download at the Copernicus Marine Service website (https://marine.copernicus.eu/).

2.3. Methods

2.3.1. Extraction of offshore wind turbines from Sentinel-1 imagery

Offshore wind turbines exhibit strong reflective signals in both optical and microwave imagery (Xu et al., 2020; Hoeser et al., 2022). Sentinel-1 microwave imagery, unaffected by clouds, offers a distinct advantage in identifying artificial targets. In this study, the extraction process for offshore wind turbines was conducted as follows: (1) Sentinel-1 VV polarization images from October to December of each year from 2016 to 2024 were collected using the Google Earth Engine (GEE) platform; (2) annual images were composited using the mean-value method to effectively reduce interference (Wang et al., 2024) from ships, aircraft, and noise; (3) Offshore wind turbines were initially extracted using a thresholding method, with the threshold set at VV (VV-polarized backscatter coefficients) ≥ -7 dB (Fig. 2); (4) The preliminary extraction results underwent a series of morphological operations, including successive 3×3 pixel window opening (erosion followed by dilation) and closing (dilation followed by erosion) operations (Meng and Xing, 2013), followed by area-based filtering ($9 \leq N \leq 120$, where N represents the number of wind turbine pixels), effectively removing isolated small patches, ghosting artifacts, and large offshore platforms while simultaneously filling voids (Fig. 2); (5) Medium and small offshore platforms were manually removed through visual inspection; (6) The centroids of wind turbines were derived based on the refined extraction results obtained through the aforementioned processing steps; (7) The "Aggregate Points" tool in ArcMap was employed with a uniform aggregation distance of 13 km to delineate the distribution area of wind turbines and compute turbine density, defined as the ratio of the number of turbines to the total area of their distribution region. It is worth noting that, in this study, offshore platforms were defined as all stationary artificial structures, excluding offshore wind turbines. Among them, platforms with diameters smaller than, similar to, or greater than the pile foundations of offshore wind turbines were classified as small, medium, and large platforms, respectively, without further distinction by specific functional purpose.

Regarding the extraction threshold of offshore wind turbines in step (3), this study determines it by analyzing the frequency histograms of VV values from typical ground object samples—wind turbines, seawater, aquaculture facilities, and tidal flats—delineated on VV composite images across different time periods and regions, as shown in Fig. 2. Notably, the VV values of wind turbines within the black box in Fig. 2 (m) are similar to those of tidal flats and farming facilities, making differentiation challenging. To prevent misidentification of tidal flats

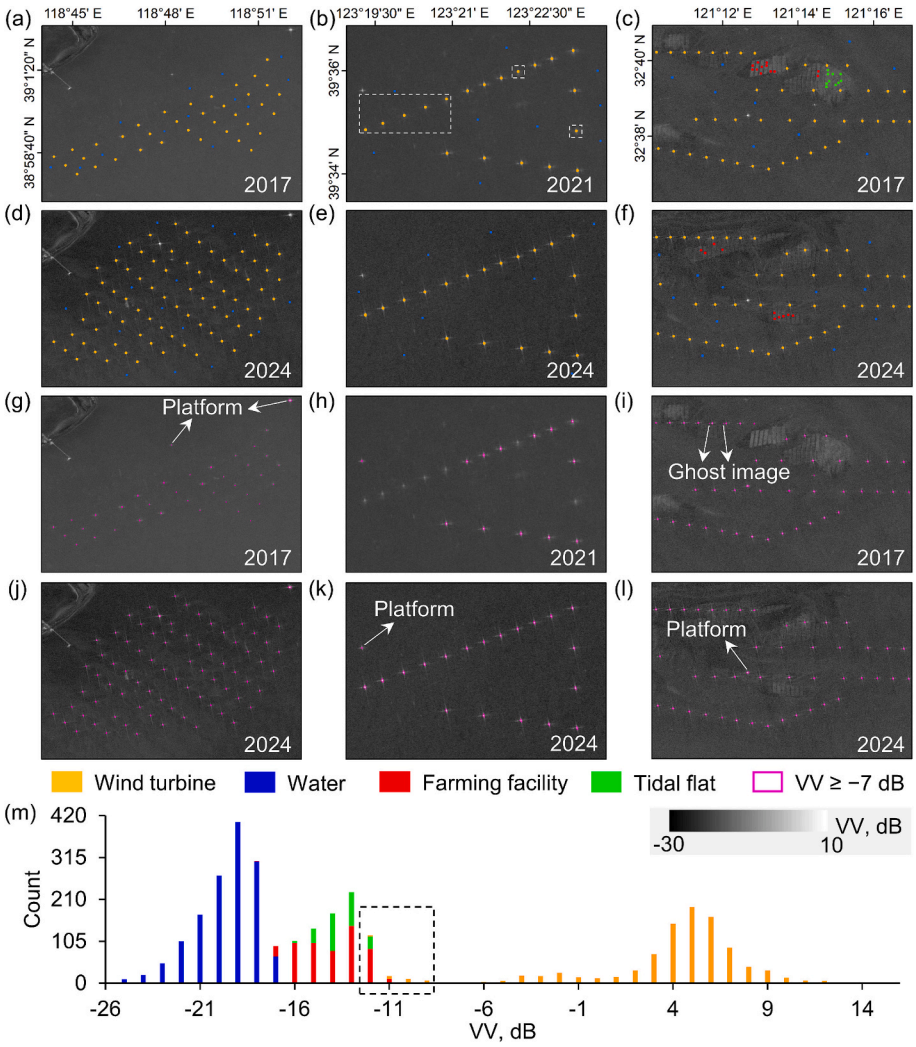

Fig. 2. Spatial distribution of samples: (a) 2017 and (d) 2024 in Caofeidian; (b) 2021 and (e) 2024 in Zhuanghe; (c) 2017 and (f) 2024 in the Jiangsu shoal. (g)-(l) Preliminary extraction results of offshore wind turbines. (m) Frequency histogram of VV values within the sample area, where the statistical results of wind turbines inside the black dashed box in (m) originate from samples within the white dashed box in (b).

and farming facilities, an extraction threshold of VV ≥ -7 dB was applied (Fig. 2(g)-(m)).

Additionally, the accuracy of the wind turbine extraction results in this study was evaluated using aerial photos and a validated wind turbine dataset published by Zhang et al. (2021). The evaluation metrics included Precision (P), Recall (R), and F1 score, as defined in Eqs. (1)–(3).

$$P = TP/(TP + FP) \tag{1}$$

$$R = TP/(TP + FN) \tag{2}$$

$$F1 = 2 \times P \times R/(P + R) \tag{3}$$

where TP represents the number of correctly identified wind turbines, FP denotes the number of erroneously identified wind turbines, and FN refers to the number of wind turbines that were missed during extraction.

2.3.2. *Extraction of offshore wind turbine water surface wakes from Sentinel-2 imagery*

Under the influence of ocean currents, wakes form around wind turbines on the sea surface (Fig. 1(c), (e), (g)). The characterization model of wind turbine wakes is crucial for wake extraction. In this study, both single-band and two-band models were utilized to conduct experiments. The single-band models included R(492) (surface reflectance at 492 nm, the Level-2A product of Sentinel-2), R(559), R(665), R(704), R(739), R(780), R(833), and R(864). The two-band models comprised [R(559) + R(665)]/[R(559)/R(665)] (Li et al., 2002), R(559)/R(492), R(665)/R(492), R(665)/R(559), R(704)/R(492), R(704)/R(559), and R(704)/R(665). Through testing, it was found that the characterization model constructed using surface reflectance data is sufficient for extracting offshore wind turbine wakes. This approach eliminates the need for SSC products and thereby avoids the additional uncertainties introduced by the SSC inversion model. The performance of the characterization models was assessed by calculating the relative difference (RD) of the coefficient of variation (CV) along profiles located on either side of the offshore wind turbines (Fig. 1(g)). A greater CV at profile L2-L2′ compared to profile L1-L1′, along with a larger RD between them, indicates enhanced sensitivity of the model to wind turbine wakes, thereby demonstrating the superior capability of the characterization model. The CV and RD values were computed using Eqs. (4) and (5), respectively.

$$CV = Std/Mean \tag{4}$$

where Std represents the standard deviation, and Mean represents the mean value.

$$RD = (CV_{L2-L2'} - CV_{L1-L1'})/CV_{L1-L1'} \quad (5)$$

where $CV_{L2-L2'}$ and $CV_{L1-L1'}$ represent the coefficient of variation of the characterization model at profiles L2-L2′ and L1-L1′, respectively.

This study introduces a wake extraction index based on the characterization model of wind turbine wakes. The wakes of wind turbines and other offshore artificial installations (platforms and ships) were extracted using threshold segmentation of the index and subsequent classification post-processing. The post-classification processing includes removal of small patches (diameter < 30 m) via majority analysis (neighborhood analysis using a 3 × 3 pixel window) and manual visual correction to enhance accuracy. Furthermore, the sliding window background smoothing technique was employed to mitigate the impact of image gradient differences during threshold segmentation, thereby improving the extraction of characteristic targets (Keesing et al., 2011; Liu et al., 2022). Based on the method described above, we propose the Scaled Index of Suspended Sediments Wake (SI-SSW) for extracting wind turbine water surface wakes, as detailed in Eq. (6).

$$SI - SSW = CM_{wake} - med(CM_{wake}) \quad (6)$$

where CM_{wake} represents the characterization model of wind turbine wake, and *med* denotes median filtering operation. The computation of the SI-SSW requires careful selection of an appropriate median filtering window. A window that is too small may result in fragmented and unrecognized wakes, while an excessively large window may lead to the inclusion of non-wake features. In this study, the optimal filtering window was determined as the one where the relative change rate (S_{rc}) of the wake extraction area, calculated between consecutive windows within the white box depicted in Fig. 1(g), was less than 2%, ensuring precise and consistent wake extraction.

The calculation of S_{rc} follows Eq. (7).

$$S_{rc} = 100\% \times (S_{i+2} - S_i)/S_i \quad (7)$$

where S_i represents the extracted area of the offshore wind turbine water surface wakes when the window size is i. i = 3, 5, 7, …, 45.

2.3.3. Estimating SSC from Sentinel-2 imagery

For SSC retrieval in the Bohai Bay and Jiangsu shoal, an inversion model was developed using in-situ SSC measurements and spectral data from the Yellow River estuary (Xing et al., 2014; Hou et al., 2023) and the Pearl River estuary (Xing et al., 2013). The SSC measured in the two estuaries and their vicinity waters ranged from 0 to 2500 mg/L, and the developed monitoring model (Eq. (8)) is suitable for a wide range of SSC, such as in the Bohai Sea and the Jiangsu shoal.

$$y = 7.219*\exp(26.173*x) \quad (8)$$

Where y represents SSC (mg/L), x is defined as [Rrs(559) + Rrs(665)]/[Rrs(559)/Rrs(665)], and Rrs(559) represents remote sensing reflectance at 559 nm. The model achieves a coefficient of determination (R^2) of 0.9119, with a Mean Absolute Percentage Error (MAPE) of 47.1%. When applying the model to Sentinel-2 satellite imagery, the Rrs was approximated using the ratio of reflectance (R) to π (Yu et al., 2012; Pahlevan et al., 2021; Zhang et al., 2023).

3. Results

3.1. Accuracy assessment for offshore wind turbines

The extraction results for wind turbines at aerial photograph locations are presented in Fig. S1. Aerial photos of Caofeidian and the western part of Bohai Bay (Fig. 1) reveal that the number of wind turbines is 75 and 24, respectively, aligning closely with the remote sensing results shown in Fig. S1(a)-(b). The wind turbine locations extracted in Jiangsu offshore waters (Fig. S1(c)) are largely consistent with visual observations from aerial photos. Additionally, the extraction results in this study were evaluated using the wind turbine validation dataset, as shown in Fig. S2. The evaluation revealed that three wind turbines near the offshore area of Zhuanghe were missed during extraction, while all other locations showed complete consistency with the validation dataset. The missed turbines were primarily due to their construction beginning in late 2019; however, they were successfully included in the wind turbine extraction results for 2020. The evaluation metrics indicate outstanding accuracy, with Precision (P) of 100%, Recall (R) of 98.81%, and an F1 score of 99.4%. This guarantees the robustness and reliability of subsequent analyses concerning the evolution of wind turbines.

3.2. Evolution of offshore wind turbines

3.2.1. The northern China coastal waters

The spatial distribution of offshore wind turbines in northern China coastal waters from 2016 to 2024 is shown in Fig. 3(a). It can be observed that the majority of offshore wind turbines are located in the coastal areas of Shandong Province and Jiangsu Province, with a greater number of turbines in the Yellow Sea compared to those in the Bohai Sea. The northernmost wind farm is located in the coastal waters of Liaoning Province, while the largest area of individual wind farm distribution is observed in the coastal waters of Jiangsu. As shown in Fig. 3 (b), from 2016 to 2024, the number and distribution area of offshore wind turbines in northern China coastal waters have shown an increasing trend, rising from 322 and 416.93 km^2 in 2016 to 3840 and 6277.21 km^2 in 2024. Furthermore, the distribution density of wind turbines showed a decreasing trend from 2016 to 2020, followed by an increasing trend from 2020 to 2024. By 2024, the wind turbine distribution density reached 0.61 units/km^2.

3.2.2. The Bohai Sea

The spatial distribution of offshore wind turbines in the Bohai Sea from 2016 to 2024 is illustrated in Fig. 4(a)-(d). These wind turbines are predominantly clustered within six wind farm regions, including three situated in the Bohai Bay, one in the southern part of Laizhou Bay, and two in the northern part of Laizhou Bay. As reported by HCIG Energy (2017), the construction of offshore wind turbines in Caofeidian, Bohai Bay, commenced in May 2016 with a planned total of 75 turbines. Satellite observations first detected the distribution of wind turbines in 2017. By 2020, satellite monitoring identified a total of 75 wind turbines near Caofeidian, a figure fully aligned with reported data.

From 2017 to 2021, offshore wind turbines in the Bohai Sea were exclusively located in the Caofeidian. In 2022, wind turbine construction expanded to the southeastern part of Bohai Bay and the southern part of Laizhou Bay. Subsequently, construction commenced in the northwest and northeast areas outside Laizhou Bay in 2023 and 2024, respectively. As shown in Fig. 4(e), the number and distribution area of wind turbines in the Caofeidian showed an increasing trend from 2017 to 2020, with little change between 2020 and 2024. The distribution density of wind turbines initially decreased, then increased, and ultimately stabilized from 2017 to 2024. By 2024, the number of wind turbines in the Caofeidian reached 75, with a distribution area of approximately 63 km^2, with a density of about 1.19 units/km^2. As shown in Fig. 4(f), the number and distribution area of wind turbines across the Bohai Sea exhibited a general upward trend from 2017 to 2024, with a pronounced increase between 2021 and 2024. Notably, a construction hiatus was observed between 2020 and 2021. Although the distribution density experienced modest increases during 2018–2021 and 2022–2024, the overall trend was a decrease. By 2024, the total number of wind turbines in the Bohai Sea had reached 444, with a distribution area of approximately 579.91 km^2, and a density of about 0.77 units /km^2.

3.2.3. The northern Yellow Sea

Offshore wind turbines in the northern Yellow Sea are primarily

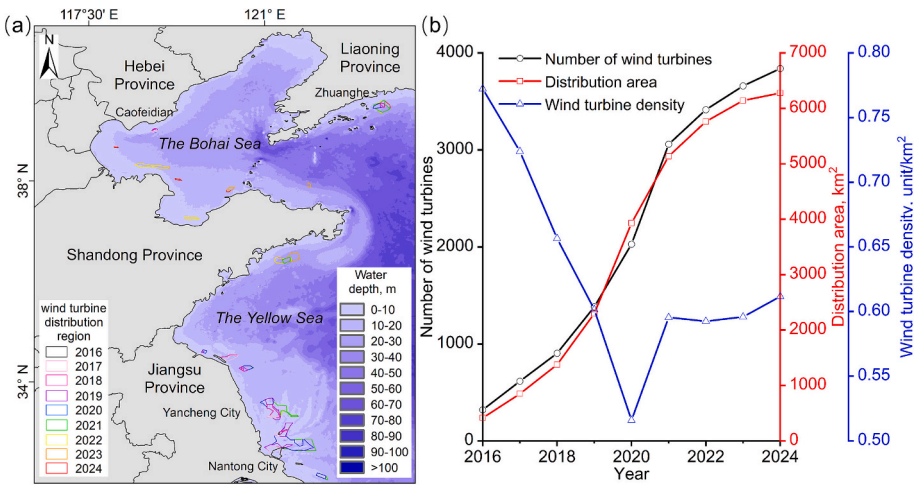

Fig. 3. (a) Spatial distribution region of offshore wind turbines in northern China coastal waters from 2016 to 2024. (b) number, distribution area, and density of offshore wind turbines in northern China coastal waters.

concentrated in two wind farm areas: the offshore region of Dalian Zhuanghe in Liaoning Province and the northern offshore area of Shandong Province, as shown in Fig. 5(a)-(c). Wind turbine construction in the northern Yellow Sea commenced in 2017, with turbines only located off the coast of Zhuanghe, until 2023. In 2023, construction expanded to the northern offshore area of Shandong Province. As shown in Fig. 5(d), the number and distribution area of wind turbines in the northern Yellow Sea demonstrated an increasing trend from 2017 to 2024. The number of wind turbines grew from 2 in 2017 to 287 in 2024. By 2024, the total distribution area of wind turbines had reached approximately 533.76 km^2. However, the distribution density of wind turbines exhibited a declining trend, decreasing from 0.87 units/km^2 in 2018 to 0.54 units/km^2 in 2024.

3.2.4. The southern Yellow Sea

The spatial distribution of offshore wind turbines in the southern Yellow Sea during 2016–2024 is illustrated in Fig. 6(a)-(i). These turbines are primarily concentrated in one offshore wind farm located in the eastern sea area of Shandong Province and seven offshore wind farms near Yancheng City and Nantong City in Jiangsu Province. Construction of offshore wind turbines in the eastern offshore area of Shandong Province commenced in 2021, with a steady annual expansion thereafter. In the northeastern sea area of Yancheng City, the construction of offshore wind turbines increased year by year from 2016 to 2020, with the number of wind turbines in the northern three wind farms remaining largely unchanged from 2020 to 2024. The majority of the offshore wind turbines are distributed in the eastern sea area of Yancheng City and the northern sea area of Nantong City, where two wind farms first emerged in 2020. These wind farms experienced further spatial expansion in 2021, followed by relative stability in their distribution. In the eastern sea area of Nantong City, there was only one wind farm from 2016 to 2019, with the construction of a second wind farm initiated in 2020.

As shown in Fig. 6(j), the number and distribution area of offshore wind turbines in Jiangsu Province generally increased from 2016 to 2021, with little change from 2022 to 2024. Over this period, the number of offshore wind turbines rose from 322 in 2016 to 2745 in 2024, while the distribution area expanded from 416.93 km^2 to 4574.95 km^2, representing approximately 9-fold and 11-fold increases, respectively. The density of offshore wind turbines decreased annually from 2016 to 2020, increased slightly in 2021, and stabilized thereafter. By 2024, the distribution density of offshore wind turbines in Jiangsu Province was approximately 0.6 units/km^2. As shown in Fig. 6(j), (k), the changes in the number, distribution area, and distribution density of offshore wind turbines in the southern Yellow Sea from 2016 to 2021 were primarily influenced by developments in Jiangsu Province. From 2021 to 2024, these changes were largely driven by developments in the eastern offshore area of Shandong Province. By 2024, the southern Yellow Sea hosted 3109 offshore wind turbines, covering a total distribution area of 5163.54 km^2, with a distribution density of 0.6 units/km^2.

3.3. Offshore wind turbine water surface wakes

3.3.1. Characterization models and spatial distribution

The statistical values of the single-band and two-band models for profiles L1-L1′ and L2-L2′ in the Bohai Bay are illustrated in Fig. S3. The corresponding mean values, standard deviation, and relative differences (RD) are presented in Table 1. Profile L2-L2′ intersects 11 wind turbine wakes. For the single-band models, the statistical value curves of models R(492), R(559), R(665), and R(704) at profile L2-L2′ exhibit 11 distinct peaks, whereas the peaks observed in models R(739), R(780), R(833), and R(864) are less pronounced. This is attributed to the strong absorption of longer light wavelengths by water (Ma et al., 2009), reducing sensitivity to wind turbine wakes. For the two-band models, at profile L2-L2′, the statistical value curves of models [R(559) + R(665)]/[R(559)/R(665)], R(559)/R(492) and R(655)/R(492) display 11 distinct peaks, while the model R(704)/R(665) exhibit 11 valleys. Regarding RD, the single-band model R(665) exhibits the highest RD (2.787), followed by the model [R(559) + R(665)]/[R(559)/R(665)], indicating that the single-band model R(665) is more effective in characterizing the wind turbine water surface wakes.

For the Bohai Bay, the characterization model R(665) was employed to construct the SI-SSW, identifying regions with SI-SSW[R(665)] $\geq$ 0.002 as preliminary offshore wind turbine wake extractions. Following classification post-processing, final wake extraction results were obtained. As the window size increases, the extracted wake area expands progressively, while the relative change rate of the area (S_{rc}) decreases (Fig. 7(b)). When S_{rc} drops below 2%, the window size is 35 × 35, corresponding to the wake extraction results shown in Fig. 7(a). In the region A of Bohai Bay (Fig. 7(a)), where wind turbine wakes minimally overlap, 34 wind turbines were identified. The average extracted area per turbine wake is approximately 0.06 km^2. The SI-SSW threshold method effectively extracts prominent wakes. However, it may fail to detect wakes that have spectra similar to seawater and lack distinct textural features, resulting in an underestimation of wake areas for offshore wind turbines. The manual visual interpretation of clearly discernible wind turbine wake areas (Fig. 7(a)) indicated that the average area of a single wind turbine wake is approximately 1.84 km^2.

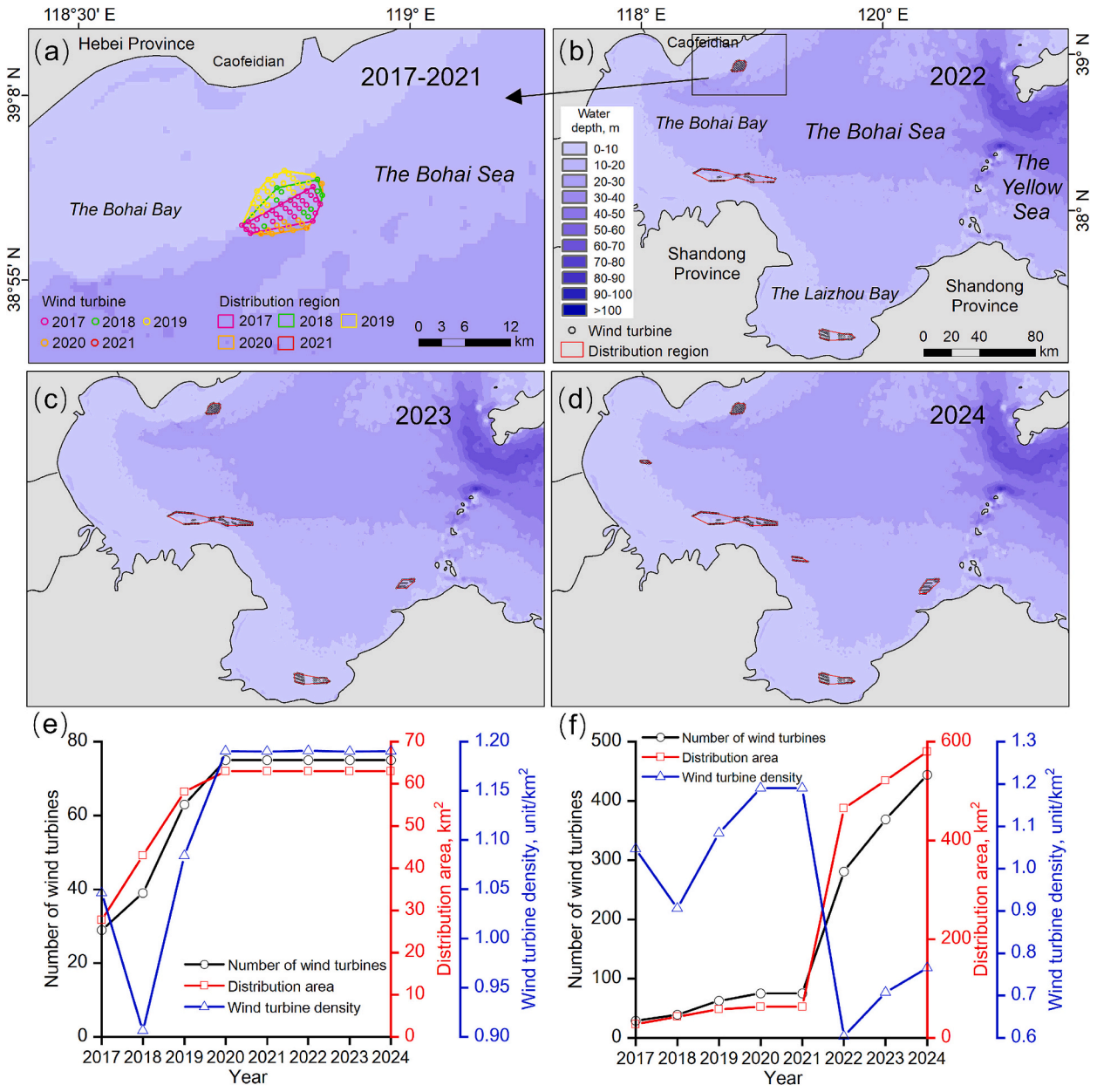

Fig. 4. (a)-(d) Spatial distribution of offshore wind turbines in the Bohai Sea from 2016 to 2024. (e) and (f) the number, distribution area, and distribution density of offshore wind turbines in the Caofeidian and the Bohai Sea, respectively.

For the extraction of the wake behind offshore wind turbines in the Jiangsu shoal, the window size of the SI-SSW[R(665)] imagery was set to 35 × 35, with the extraction threshold finely tuned to 0.006. After classification and post-processing, the results are presented in Fig. 7(c). Three non-overlapping wind turbine wakes were identified (Fig. 7(d)). The average wake area extracted using the SI-SSW threshold method was approximately 0.34 km^2, with an average wake length of 5.59 km. In comparison, the wake area identified through visual interpretation averaged 0.48 km^2, with a length of about 5.63 km (Fig. 7(d)). In the Jiangsu shoal, the difference between the wake areas extracted using the SI-SSW threshold method and visual interpretation is relatively small. However, the wake area extracted by the threshold method in the Jiangsu shoal is larger than that in the Bohai Bay in our study. The wake area extracted using the threshold method was considered as the significantly affected area of a single offshore wind turbine on SSC, while the wake area interpreted visually was taken as the total affected area. The results show that the significantly affected area of a single offshore wind turbine on SSC can exceed 0.3 km^2, whereas the total affected area surpasses 1.5 km^2. By 2024, the total significantly affected area (calculated as the number of wind turbines multiplied by the significantly affected area per turbine) of offshore wind farms on SSC exceeds 100 km^2 in the Bohai Sea and 900 km^2 in the southern Yellow Sea.

3.3.2. *The suspended sediments concentration (SSC)*

The SSC distributions in wind farms of the Bohai Bay and the Jiangsu shoal are shown in Fig. 8(a)-(c). In the Bohai Bay, the tidal level was approximately 82 cm with the overflight of Sentinel-2, corresponding to the flood tide phase, with a surface current velocity of approximately 0.25 m/s. The SSC of the wind turbine wake extracted using the SI-SSW threshold method (A1-A5 in Fig. 8(a), Table 2) averaged approximately 11.1 mg/L, which is about 8.77% higher than that of the surrounding normal water bodies (a1-a5). For the wind turbine wake manually extracted (A6), the SSC was approximately 9.96 mg/L, which is about

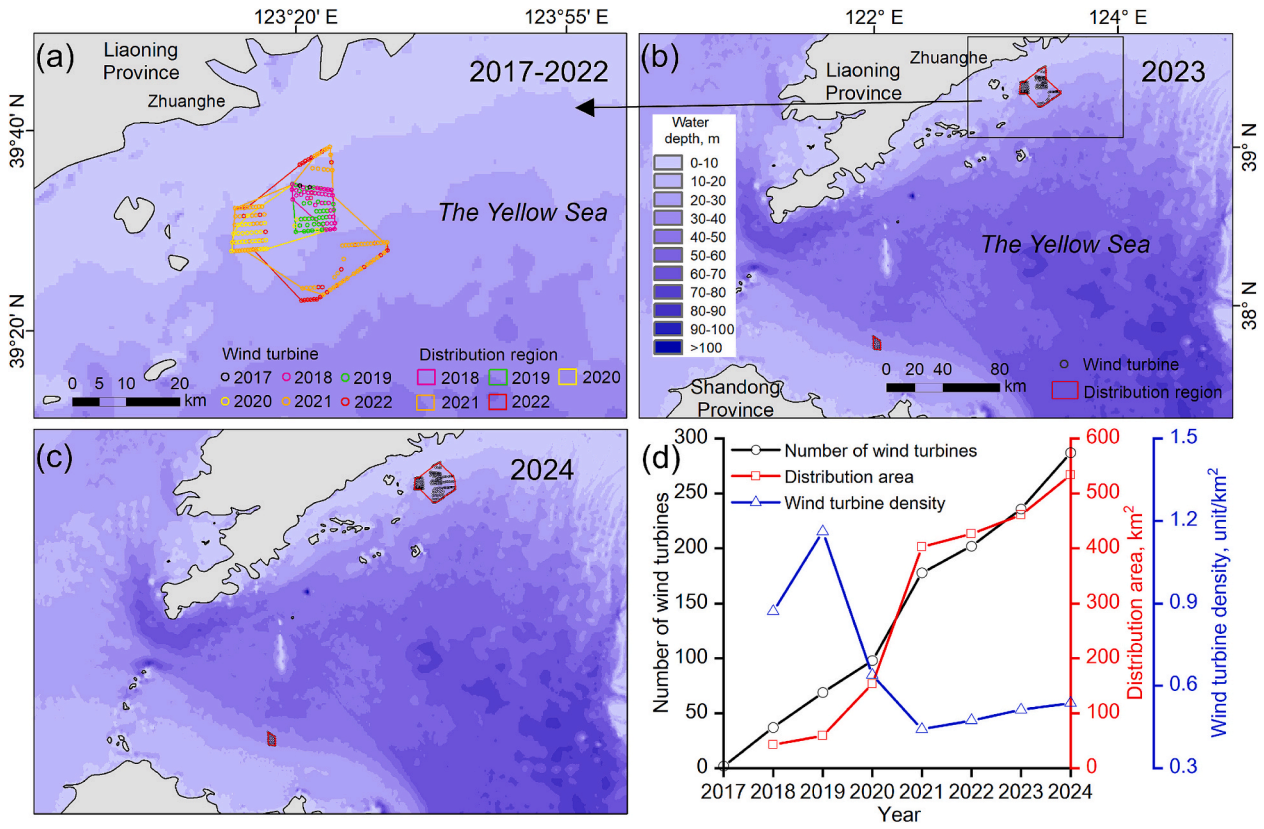

Fig. 5. (a)-(c) Spatial distribution of offshore wind turbines in the northern Yellow Sea from 2017 to 2024. (d) Number, distribution area, and distribution density of wind turbines in the northern Yellow Sea.

2.23% higher than that of the normal water bodies (a6). The SSC in the Jiangsu shoal (Fig. 8(b)) is generally higher than that in the southern nearshore wind farm areas of the Bohai Bay. During the satellite pass, the tidal level at the nearby station (Dafeng Port) was approximately 394 cm, corresponding to the flood tide phase, with a surface current velocity of around 0.05 m/s. Under these conditions, the average SSC in the wake water extracted using the SI-SSW threshold method was approximately 109.88 mg/L (A7-A9 in Fig. 8(b), Table 2), representing a 44.27% increase compared to the surrounding normal water (a7-a9). The SSC in the wake water, as determined through visual interpretation, was approximately 101.1 mg/L (A10-A12 in Fig. 8(c), Table 2), showing a 32.75% increase relative to normal water. Overall, the SSC within wind turbine wakes is, on average, approximately 22.01% higher than that of the surrounding water bodies.

The SSC in the downstream wake is significantly higher than that in the upstream water body (Fig. 8(d), (f)). For instance, at the 4531 m position in Fig. 8(d), the SSC along the downstream profile L7-L7′ (13.14 mg/L) is notably higher than that along the upstream profile L5-L5′ (10.28 mg/L). The number of SSC peaks observed in the downstream profile corresponds to the number of upstream wind turbines. Along the extension direction of the wind turbine wake, the SSC in the wake water body generally exhibits a decreasing trend with increasing distance from the wind turbine (Fig. 8(e), (g)). In Bohai Bay, from east to west, the SSC within turbine wakes generally exhibits an increasing trend, accompanied by an increasing influence range of the wake. The length of suspended sediment wakes downstream of wind turbines in the Bohai Bay exceeds 1.5 km, while those observed offshore of Jiangsu shoal are even longer, extending beyond 5 km.

4. Discussion

4.1. Characteristics of offshore wind turbine water surface wakes

As shown in Figs. S4, S5, the extension direction of the wind turbine wake exhibits significant spatiotemporal variability. Statistical analysis reveals a strong correlation between the wake extension direction and tidal conditions, consistent with the findings of Bailey et al. (2024). In the southern Bohai Bay, 35 cloud-free satellite images from 2023 were analyzed. Among them, 27 images indicated that during flood tides, the wake extension direction was northwestward, while during ebb tides, it was southeastward. This pattern is particularly evident during rapid flood or ebb tides, as shown in Fig. S5(a), (b). The distinct peaks in the profiles shown in Fig. S6(a), (b), along with the absence of significant peaks in Fig. S6(d), further corroborate this observation. Eight images showing wake extension directions that differ from the above patterns were found, but their tidal conditions were similar to those on April 19, 2023, and August 4, 2023 (Fig. S5(c), (d)), which were in the slack water stages of the tide. The difference may be attributed to the fact that during slack water stages, the timing of the flow direction reversal does not always correspond exactly with the moments of tidal extremes (Yu and Zhang, 2017). In the Caofeidian, 46 images from 2023 were analyzed. Among these, 44 images indicated that during flood tides, the wake extension direction was southwestward, while during ebb tides, it was northeastward. This phenomenon was more pronounced during rapid flood or ebb tides (Figs. S5(e)-(f), S6(e)-(f)). Only two images (Figs. S5(g)-(h), S6(g)-(h)) during the slack ebb stage showed a deviation from this pattern.

There are significant variations in the SSC of wake water depending on the location of the offshore wind turbines. Taking the wind turbines extracted from Region A in Fig. 7(a) as an example, the relatively small display area allows for the assumption of uniform surface current

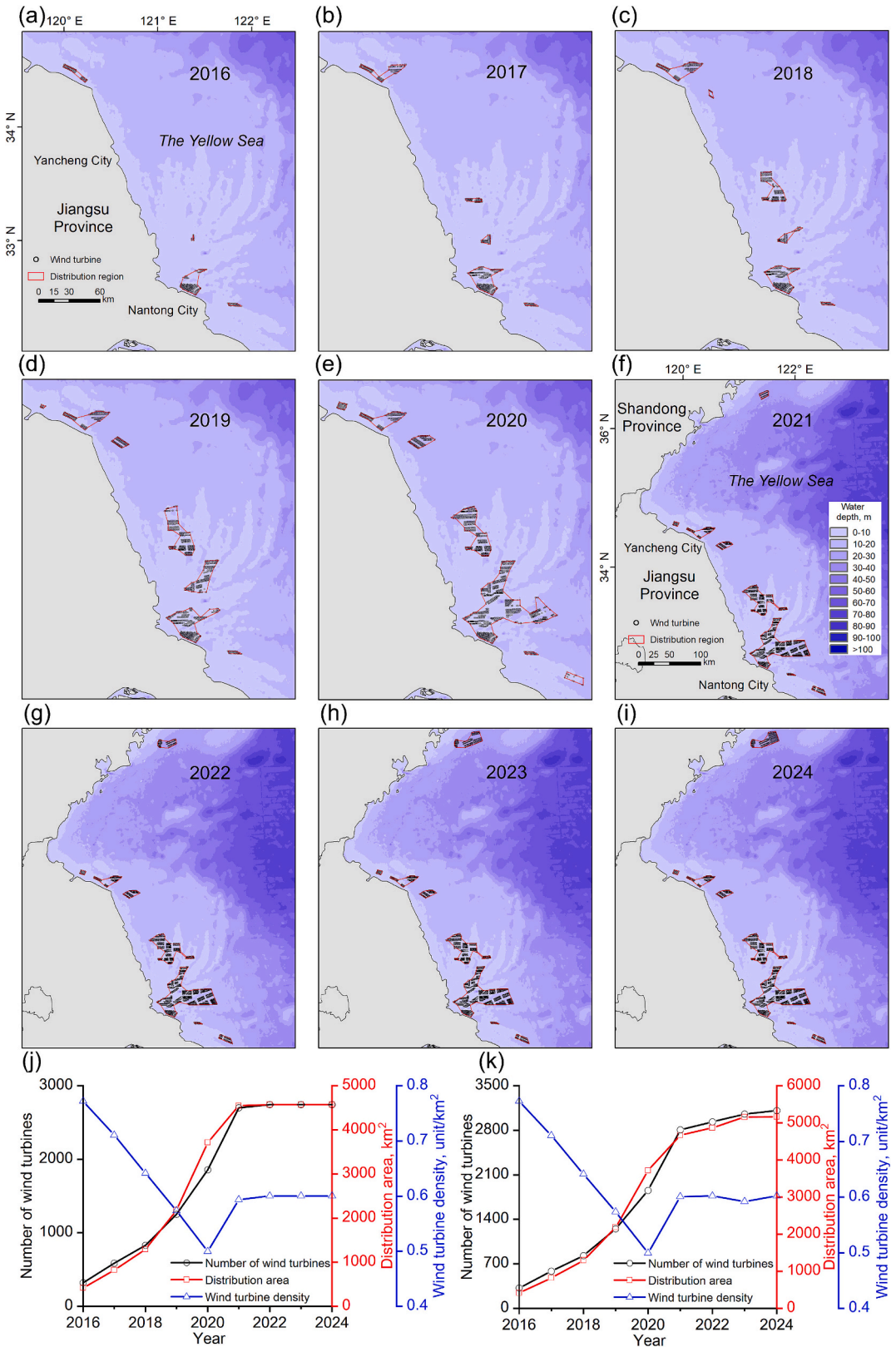

Fig. 6. (a)-(i) Spatial distribution of offshore wind turbines in the southern Yellow Sea from 2016 to 2024. (j) and (k) the number, distribution area, and distribution density of offshore wind turbines in the offshore area of Jiangsu Province and the southern Yellow Sea, respectively.

Table 1
Mean values, standard deviation (Std), and relative difference (RD) of the characterization models at profiles L1-L1′ and L2-L2′.

Characterization Model	Mean (L1-L1′)	Mean (L2-L2′)	Std (L1-L1′)	Std (L2-L2′)	RD	Characterization Model	Mean (L1-L1′)	Mean (L2-L2′)	Std (L1-L1′)	Std (L2-L2′)	RD
R(492)	0.0685	0.0691	0.0026	0.0054	1.0892	[R(559) + R(665)]/[R(559)/R(665)]	0.0408	0.0417	0.0019	0.0071	2.6172
R(559)	0.0656	0.0677	0.0030	0.0078	1.5553	R(559)/R(492)	0.9579	0.9781	0.0296	0.0459	0.5199
R(665)	0.0284	0.0291	0.0012	0.0045	2.787	R(665)/R(492)	0.4154	0.4194	0.0163	0.0351	1.1276
R(704)	0.0254	0.0251	0.0009	0.0031	2.3798	R(665)/R(559)	0.4338	0.4285	0.0176	0.0234	0.3516
R(739)	0.019	0.0174	0.0007	0.0015	1.1966	R(704)/R(492)	0.3709	0.3627	0.0154	0.024	0.59
R(780)	0.0189	0.0173	0.0007	0.0015	1.2631	R(704)/R(559)	0.3875	0.371	0.0174	0.0214	0.2837
R(833)	0.0159	0.0144	0.0008	0.0015	0.9543	R(704)/R(665)	0.8937	0.8673	0.0365	0.0513	0.4464
R(865)	0.0155	0.0139	0.0008	0.0014	0.9957	–	–	–	–	–	–

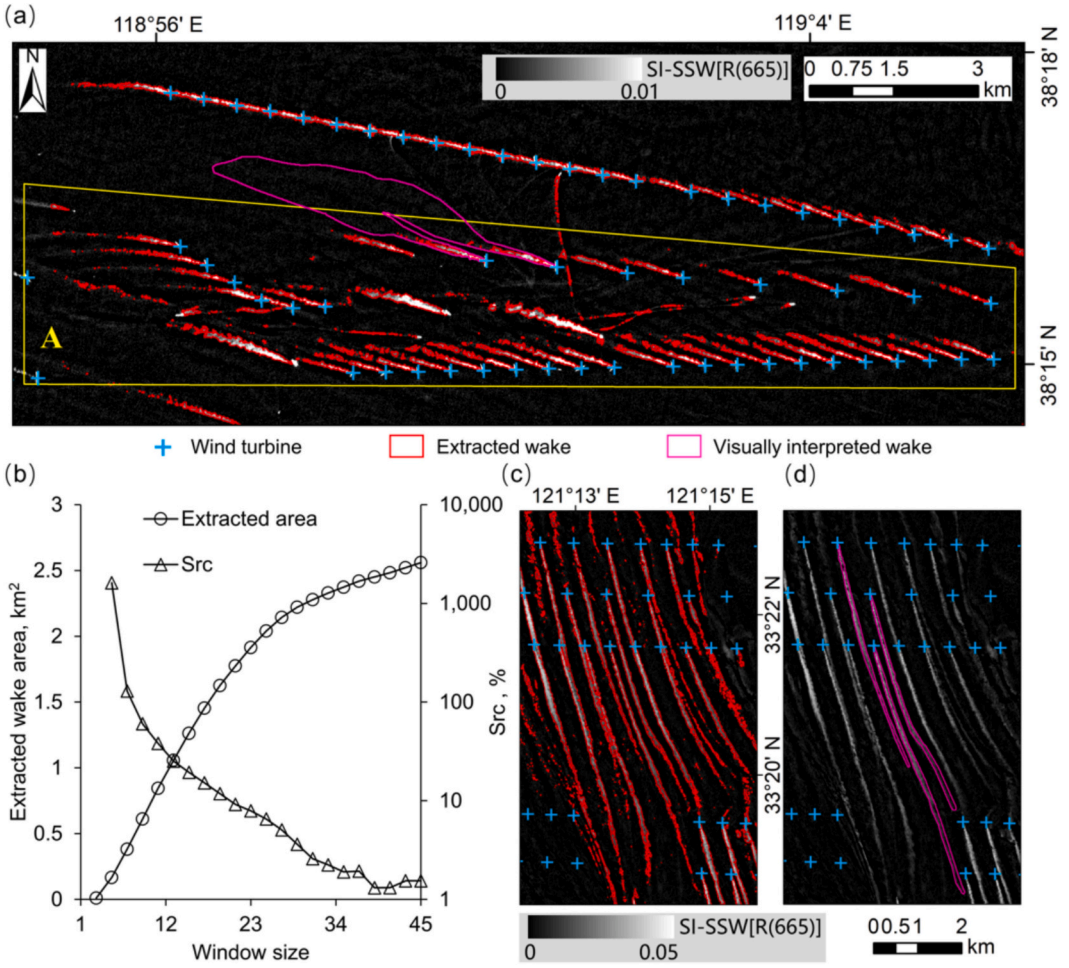

Fig. 7. Extraction results of offshore wind turbine water surface wakes in the (a) Bohai Bay and (c)-(d) the Jiangsu shoal, with a window size of 35 × 35, are shown for the dates August 14, 2023, and May 23, 2023, respectively. The base maps are SI-SSW[R(665)] imagery. (b) The wake extraction area (within the white box in Fig. 1(g)) and its relative change rate (S_{rc}) under different window sizes.

velocity. From east to west, the SSC of offshore wind turbine water surface wakes generally increases (Fig. 8(a)), while the water depth decreases (Fig. 9(a)). The correlation coefficient between water depth and SSC in wind turbine wakes, extracted via the SI-SSW threshold method, is −0.72, indicating a significant negative correlation (Fig. 9(c)). A direct comparison of wake SSC among wind turbines located at three different water depths further corroborates this pattern (Fig. 9(d)). Although the surface current velocity within the wind turbine area shown in Fig. 9(b) is lower than that in Fig. 9(a), the water depth of the wake at F3 is approximately 8 m shallower than that at F1, resulting in a higher wake SSC at F3 than at F1. However, when the difference in water depth is less than 5 m, wake SSC may be predominantly controlled by current velocity, leading to a slightly lower SSC in the relatively shallow-water wake (F3) than in the relatively deeper-water wake (F2). These findings suggest that under uniform surface current velocity, SSC variations in offshore wind turbine wake water are likely influenced by water depth. Shallower water conditions facilitate the lifting of sediment by wake vortices to the surface, resulting in elevated SSC levels within the wake water (Bailey et al., 2024; Lecordier et al., 2025; Ou et al., 2022).

Significant differences are observed in the extension direction, area, and SSC of wakes generated by different offshore installations, including wind turbines, platforms, and ships. Taking the wakes extracted via the SI-SSW threshold method (Fig. 8(a)) as an example, both offshore wind

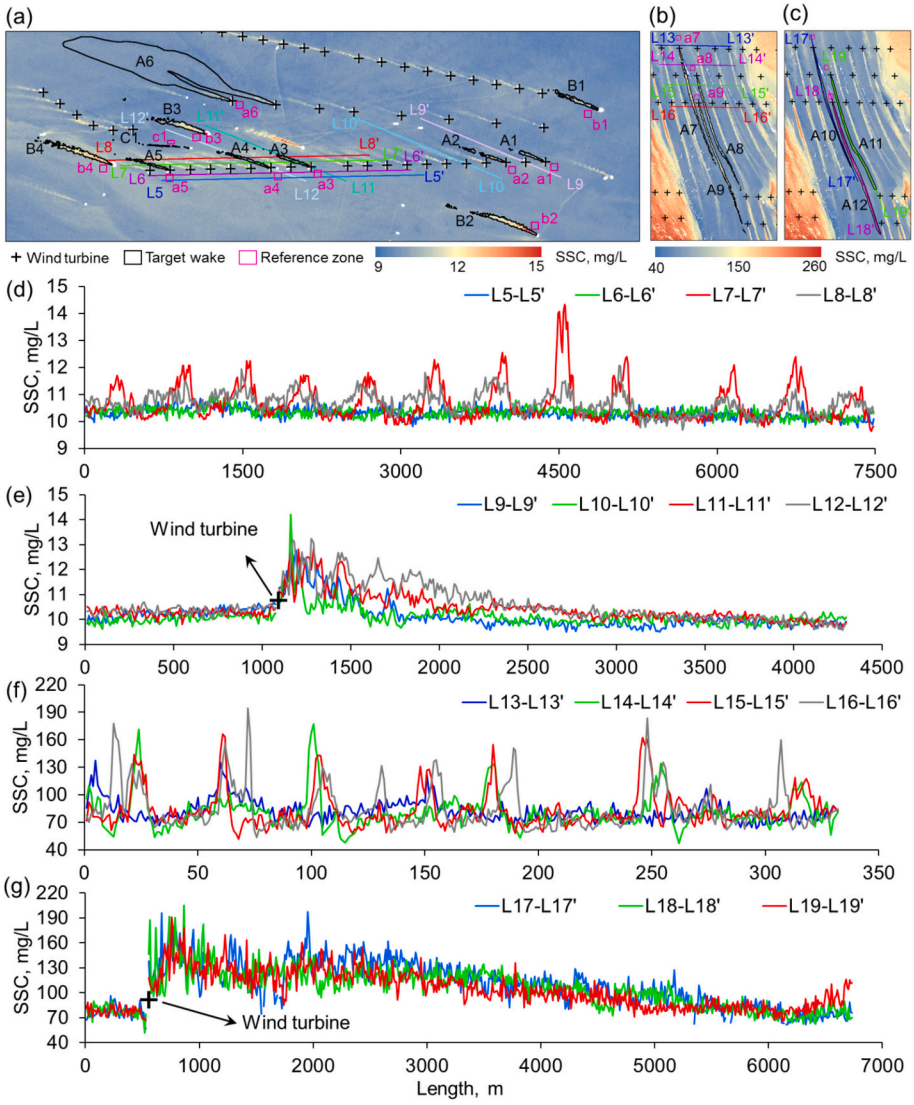

Fig. 8. (a)-(c) Distribution of SSC in the Bohai Bay and the Jiangsu shoal, along with wakes of offshore installations, reference area samples, and profiles. A1-A12 and a1-a12 represent wake and reference area samples of offshore wind turbines (A6, A10-A12 correspond to visually interpreted wakes), B1-B4 and b1-b4 represent wake and reference area samples of large offshore platforms, and C1 and c1 represent wake and reference area samples of ships. (d)-(g) SSC statistics along profiles.

Table 2
Mean SSC of offshore installations wakes and reference zones are shown in Fig. 8.

Site										
	Wake	A1	A2	A3	A4	A5	A6	A7	A8	A9
	Reference	a1	a2	a3	a4	a5	a6	a7	a8	a9
	Wake	A10	A11	A12	B1	B2	B3	B4	C1	–
	Reference	a7	a8	a9	b1	b2	b3	b4	c1	–
SSC (mg/L)	Wake	10.72	10.85	11.18	11.33	11.39	9.96	113.17	105.83	110.64
	Reference	10.00	10.10	10.24	10.31	10.35	9.74	76.18	75.74	76.57
	Wake	107.15	97.19	98.96	10.59	11.65	10.99	11.85	10.46	–
	Reference	76.18	75.74	76.57	9.93	10.01	10.00	10.55	9.93	–

turbines and large offshore platforms, being stationary targets, exhibit similar wake extension characteristics within limited areas. Conversely, wakes of non-stationary targets such as ships primarily extend in the opposite direction to the ship's movement (Caplier et al., 2020; Fan et al., 2019). The average extracted wake area for a platform is approximately 0.17 km^2, roughly three times larger than that of wind turbines, while ship wakes have an average extracted area of approximately 0.019 km^2, one-third the size of wind turbine wakes. The average SSC in the wake waters of offshore wind turbines, large offshore platforms, and ships is approximately 11.1 mg/L, 11.27 mg/L, and 10.46 mg/L, respectively (Table 2), corresponding to increases of approximately 8.77%, 11.35%, and 5.34% compared to the reference water bodies. The differences in wake area and SSC among different offshore installations may be attributed to their volumetric dimensions (ICF, 2021; Lecordier et al., 2025), with larger installations generally producing more extensive wake areas and higher SSC values. Similarly, offshore wind turbines with larger fixed foundations tend to generate larger wake areas and higher SSC values.

Furthermore, the density of offshore wind turbines may influence the duration of suspended sediment wakes. When the wind turbine density

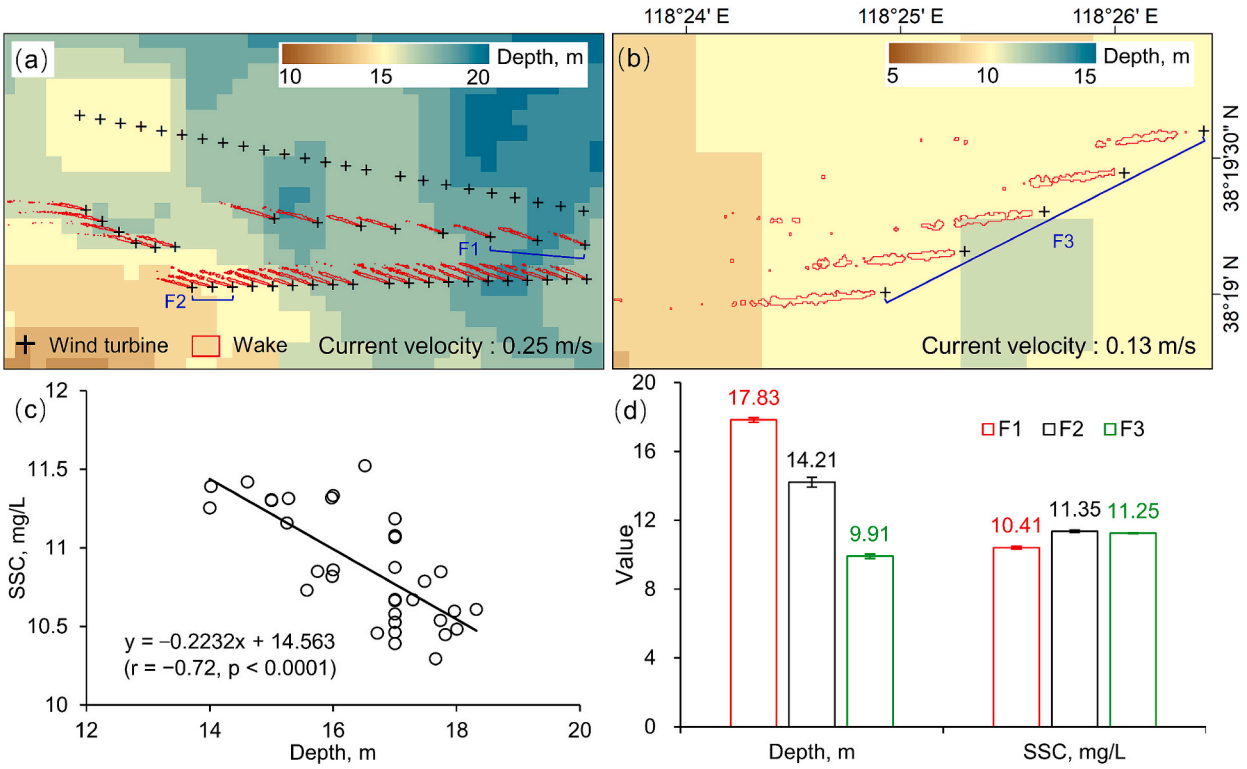

Fig. 9. (a)-(b) Distribution of water depth. (c) Relationship between water depth and wind turbine wake SSC in (a). (d) Wind turbine wake SSC versus water depth for turbines F1–F3 shown in (a)–(b).

is relatively high, the sediment wakes from multiple turbines can overlap, as seen in the first wake on the right side of A11 in Fig. 8(c), which leads to an increased duration of sediment suspension. As of 2024, the wind turbine densities in the Bohai Sea, northern Yellow Sea, and southern Yellow Sea are 0.77, 0.54, and 0.6 units/km^2, respectively. To some extent, when current velocity and water depth are comparable across regions, the suspended sediment wakes generated by wind turbines in the Bohai Sea may persist for a relatively longer duration, whereas those in the northern Yellow Sea tend to dissipate more quickly. Therefore, wind turbine density could be a critical factor to consider in future comprehensive environmental impact assessments of offshore wind farms.

4.2. Limitations of offshore wind turbines extraction and development characteristics in northern China coastal waters

Temporal variations in the construction phases of offshore wind farms significantly influence the intensity of backscatter signals from wind turbines in VV polarization composite imagery, thereby influencing the accuracy of wind turbine extraction results based on the proposed threshold (VV ≥ -7 dB). Statistical analysis indicates that 28 VV-polarized images were available for the study region in Fig. 2(b) from October to December 2021. Among them, only 13 images captured wind turbines within the white box, accounting for less than half of the total images. Furthermore, no wind turbines were detected in images acquired on or before November 15. Due to the short duration of wind turbine presence, their VV values remain low, making it difficult to distinguish them from farming facilities or tidal flats (Fig. 2(m)). Overall, for annual monitoring of wind turbines in any sea area, the method proposed in this paper can reliably detect all offshore wind turbines completed between October and December of each year. Offshore wind turbines under construction during the period from October to December of the current year are generally missed in the extraction process but will be accurately identified in the following year. Offshore wind turbines still under construction during October to December of the current year should be attributed to the following year's annual report.

Offshore wind turbines in northern China coastal waters are primarily constructed in nearshore areas with an average water depth of less than 20 m, as shown in Fig. 10(a), (b). From 2016 to 2024, the average water depth at these wind turbine locations has shown a general increasing trend. In the Bohai Sea (Fig. 10(d), (e)), the average water depth of wind turbine installation sites has generally decreased from 2016 to 2024. By 2024, the average water depth at these locations is approximately 12.57 m, with the majority of depth ranging from 5 to 20 m. In contrast, the average water depths at wind turbine installation sites in the northern Yellow Sea and southern Yellow Sea have shown an overall increasing trend from 2016 to 2024 (Fig. 10(g), (j)). Over the past nine years, the average water depth at wind turbine installation sites in the northern Yellow Sea has consistently exceeded 10 m, while in the southern Yellow Sea, it has remained below 15 m. The counts of water depths at wind turbine locations in 2024 clearly illustrate these consistent patterns (Fig. 10(h), (k)). The water depth at wind turbine installation sites is likely influenced by factors such as foundation type and construction costs. In northern China coastal waters, the majority of offshore wind turbines utilize pile-based fixed foundations, which are typically suitable for water depths of less than 50 m for installation (Li et al., 2022). Although the construction cost of offshore wind turbines in deep waters is relatively high, these regions possess significantly richer wind energy resources, with nearly 80% of the world's offshore wind potential located in waters deeper than 60 m (Huang et al., 2021). This resource advantage is corroborated by the installation trend observed between 2016 and 2024, as offshore wind turbines in northern China coastal waters have progressively extended farther into deep-sea areas, a tendency particularly evident in the Yellow Sea (Fig. 10(c), (f), (i), (l)). In deeper waters, sediment suspension caused by wake vortices from wind turbines is less likely to reach the sea surface, resulting in a relatively lower impact on SSC compared to nearshore wind turbines

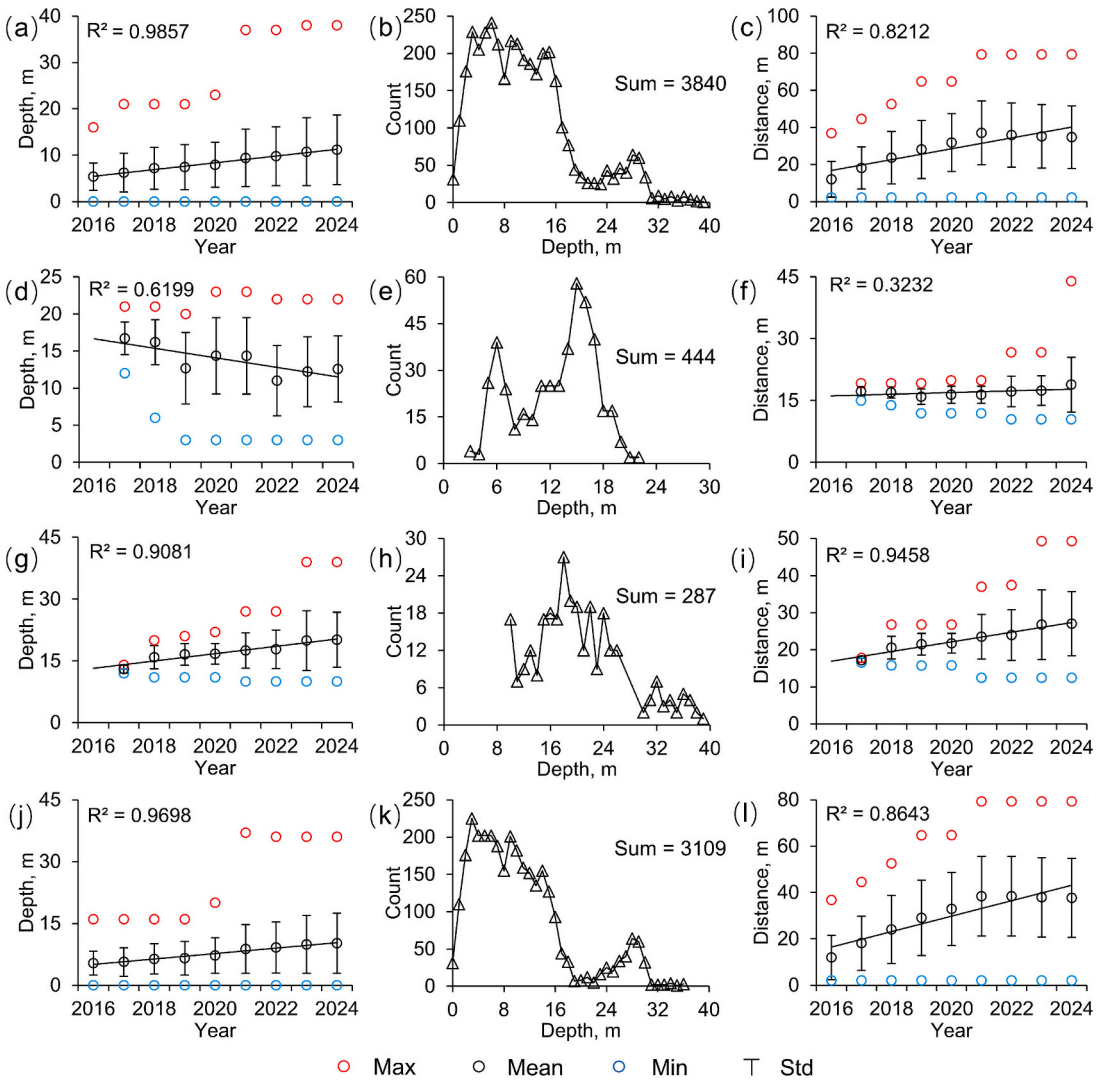

Fig. 10. The water depths at wind turbine locations in (a) northern China coastal waters, (d) the Bohai Sea, (g) the northern Yellow Sea, (j) the southern Yellow Sea from 2016 to 2024. The counts of water depths at wind turbine locations in (b) the northern China coastal waters, (e) the Bohai Sea, (h) the northern Yellow Sea, (k) the southern Yellow Sea for the year 2024. The distances from wind turbine locations to the shoreline in (c) northern China coastal waters, (f) the Bohai Sea, (i) the northern Yellow Sea, (l) the southern Yellow Sea from 2016 to 2024. (For interpretation of the references to color in this figure legend, the reader is referred to the web version of this article.)

(Lecordier et al., 2025; Ou et al., 2022). Furthermore, with the maturation of floating wind turbine technology (Li et al., 2021; Yu, 2024), the transition from nearshore to deep-sea installations is an inevitable progression for offshore wind development. Floating offshore wind turbines can effectively utilize the abundant wind energy resources in deep waters. They require relatively small seabed anchors which, although they may impact the seabed environment to some extent, result in significantly lower overall environmental impact compared to fixed foundations offshore wind turbines (Maxwell et al., 2022; ORE Catapult and ARUP, 2024). Consequently, the rapid development of floating offshore wind turbines is of great significance for the sustainable development of marine resources.

5. Conclusions and prospects

Based on remote sensing monitoring of offshore wind turbines and their water surface wakes in northern China coastal waters, this study evaluates the impact of offshore wind turbines on suspended sediment concentration (SSC). The findings indicate that, by 2024, the number and distribution area of offshore wind turbines in northern China coastal waters had increased by more than tenfold compared to 2016, with wind turbines gradually expanding towards the deep sea. The construction of the Scaled Index of Suspended Sediments (SI-SSW) using red band reflectance improved the detection of wind turbine water surface wakes. The affected area by one single offshore wind turbine on SSC ranged from 0.3 km^2 to 1.5 km^2, with SSC increasing over 20%. During strong tidal flood or ebb phases in shallower waters, larger wind turbines exert an even stronger influence on SSC within the downstream wake waters.

The data, methods and findings in this work can serve as references for the operational management of existing wind farms and for impact assessments in future wind farm development planning. Future work will build upon the findings of this study to further analyze the impacts of offshore wind turbines on other aquatic parameters, such as water temperature, water transparency, and chlorophyll concentration, achieving a comprehensive assessment of the environmental effects of offshore wind turbines on the aquatic ecosystem.

CRediT authorship contribution statement

Yingzhuo Hou: Writing – review & editing, Writing – original draft,

Software, Methodology, Formal analysis, Data curation. **Dingfeng Yu:** Writing – review & editing, Funding acquisition. **Qianguo Xing:** Writing – review & editing, Writing – original draft, Supervision, Resources, Project administration, Methodology, Funding acquisition, Formal analysis, Data curation, Conceptualization. **Shanshan Jiang:** Writing – review & editing. **Rongda Guan:** Writing – review & editing. **Maham Arif:** Writing – review & editing. **Xiangyang Zheng:** Writing – review & editing. **Jianmin Zhao:** Writing – review & editing.

Declaration of competing interest

The authors declare that they have no known competing financial interests or personal relationships that could have appeared to influence the work reported in this paper.

Acknowledgments

This work was financially supported by the National Natural Science Foundation of China [grant numbers 42476175, 42106172]; the Shandong Province Innovation Technology Guidance Plan [grant number YDZX2024021]; the Seed Project of Yantai Institute of Coastal Zone Research, Chinese Academy of Sciences [grant number YICE351030601]; the Natural Science Foundation of Shandong Province [grant number ZR2024MD003]; the Open Fund of Shandong Key Laboratory of Marine Ecological Environment and Disaster Prevention and Mitigation [grant number 202302]; Major Innovation Project for the Science Education Industry Integration Pilot Project of Qilu University of Technology (Shandong Academy of Sciences) [grant number 2023JBZ03].

Appendix A. Supplementary data

Supplementary data to this article can be found online at https://doi.org/10.1016/j.marpolbul.2026.119450.

Data availability

Data will be made available on request.

References

Baeye, M., Fettweis, M., 2015. In situ observations of suspended particulate matter plumes at an offshore wind farm, southern North Sea. Geo-Mar. Lett. 35, 247–255. https://doi.org/10.1007/s00367-015-0404-8.

Bailey, L.P., Dorrell, R.M., Kostakis, I., McKee, D., Parsons, D., Rees, J., Strong, J., Simmons, S., Forster, R., 2024. Monopile-induced turbulence and sediment redistribution form visible wakes in offshore wind farms. Front. Earth Sci. 12, 1383726. https://doi.org/10.3389/feart.2024.1383726.

Bernardo, N., do Carmo, A., Park, E., Alcântara, E., 2019. Retrieval of suspended particulate matter in inland waters with widely differing optical properties using a semi-analytical scheme. Remote Sens. 11, 2283. https://doi.org/10.3390/rs11192283.

Brandao, I.L.S., van der Molen, J., van der Wal, D., 2023. Effects of offshore wind farms on suspended particulate matter derived from satellite remote sensing. Sci. Total Environ. 866, 161114. https://doi.org/10.1016/j.scitotenv.2022.161114.

Cai, L.N., Hu, Q.F., Qiu, Z.F., Yin, J., Zhang, Y.Z., Zhang, X.K., 2023. Study on the impact of offshore wind farms on surrounding water environment in the Yangtze estuary based on remote sensing. Remote Sens. 15, 5347. https://doi.org/10.3390/rs15225347.

Caplier, C., Rousseaux, G., Calluaud, D., David, L., 2020. Effects of finite water depth and lateral confinement on ships wakes and resistance. J. Hydrodyn. 32, 582–590. https://doi.org/10.1007/s42241-019-0054-9.

Chen, Q., Tang, S.L., Wu, J., 2022. Spatial-temporal variation of suspended sediment in the Pearl River estuary retrieved from GF-4 satellite data. J. Trop. Oceanogr. 41, 65–76. https://doi.org/10.11978/2021034.

Chu, Y.H., Wu, W.J., Li, P., Chen, S.L., 2022. Temporal and spatial dynamics of suspended sediment and its driving mechanism in the Yellow River estuary. Haiyang Xuebao 44, 150–163. https://doi.org/10.12284/hyxb2022059.

CREIA (Chinese Renewable Energy Industries Association), 2023. Review and prospect of offshore wind power 2023. https://cpnn.com.cn/news/baogao2023/202307/t20230707_1616113.html (accessed 10 March 2024).

CREIA (Chinese Renewable Energy Industries Association), 2024. Review and prospect of offshore wind power 2024. https://wind.in-en.com/html/wind-2453014.shtml (accessed 5 March 2025).

Cui, R.G., Guo, J., Cheng, L.H., Zhang, Y.X., Liu, W., 2021. Status and trends analysis of global clean energies. Acta Geosci. Sin. 42, 179–186. https://doi.org/10.3975/cagsb.2020.090401.

Dincer, I., Acar, C., 2015. A review on clean energy solutions for better sustainability. Int. J. Energy Res. 39, 585–606. https://doi.org/10.1002/er.3329.

Fan, S.G., Zhang, W., Wang, D.Q., 2018. Construction organization and control of large volume cast-in-place concrete for offshore wind farm foundation project in Puti Island, Tangshan, Hebei province. Dual Use Technol. Prod. 16, 231–232. https://doi.org/10.3969/j.issn.1009-8119.2018.16.218.

Fan, K.G., Zhang, H.G., Liang, J.J., Chen, P., Xu, B.J., Zhang, M., 2019. Analysis of ship wake features and extraction of ship motion parameters from SAR images in the Yellow Sea. Front. Earth Sci. 13, 588–595. https://doi.org/10.1007/s11707-018-0743-7.

Fang, X.R., Wen, Z.F., Chen, J.L., Wu, S.J., Huang, Y.Y., Ma, M.H., 2019. Remote sensing estimation of suspended sediment concentration based on random forest regression model. Natl. Remot. Sens. Bull. 23, 756–772. https://doi.org/10.11834/jrs.20197498.

Feng, Y.Y., Zhou, Q.L., Liu, Y.J., Miao, F., Zhang, X.M., Zhang, H.J., Li, F., 2023. Impact of marine ranching and offshore wind power industrial convergence projects on marine environment. Environ. Prot. Sci. 49, 69–74. https://doi.org/10.16803/j.cnki.issn.1004-6216.2022040031.

Fu, Q., Zhang, H.X., 2024. Xinhuaboye Net, How Is the Development of the Wind Power Industry in Jiangsu? This Report Reveals the Details. https://www.xhby.net/content/s66deda76e4b0ac1d26c22338.html (accessed 1 December 2024).

Han, B., Loisel, H., Vantrepotte, V., Mériaux, X., Bryère, P., Ouillon, S., Dessailly, D., Xing, Q.G., Zhu, J.H., 2016. Development of a semi-analytical algorithm for the retrieval of suspended particulate matter from remote sensing over clear to very turbid waters. Remote Sens. 8, 211. https://doi.org/10.3390/rs8030211.

HCIG Energy, 2017. Commencement of main construction at Leiting Putidao offshore wind farm. https://www.jei.com.cn/portal/article/index/id/163/cid/7.html (accessed 12 December 2024).

He, X.Q., Bai, Y., Pan, D.L., Huang, N.L., Dong, X., Chen, J.S., Chen, C.T.A., Cui, Q.F., 2013. Using geostationary satellite ocean color data to map the diurnal dynamics of suspended particulate matter in coastal waters. Remote Sens. Environ. 133, 225–239. https://doi.org/10.1016/j.rse.2013.01.023.

Hendriks, E., Langedock, K., van Duren, L.A., Vanaverbeke, J., Boone, W., Soetaert, K., 2025. The impact of offshore wind turbine foundations on local hydrodynamics and stratification in the Southern North Sea. Front. Mar. Sci. 12, 1619577. https://doi.org/10.3389/fmars.2025.1619577.

Hernandez, O.M., Shadman, M., Amiri, M.M., Silva, C., Estefen, S.F., La Rovere, E., 2021. Environmental impacts of offshore wind installation, operation and maintenance, and decommissioning activities: A case study of Brazil. Renew. Sust. Energ. Rev. 144, 110994. https://doi.org/10.1016/j.rser.2021.110994.

Hoeser, T., Feuerstein, S., Kuenzer, C., 2022. DeepOWT: a global offshore wind turbine data set derived with deep learning from Sentinel-1 data. Earth Syst. Sci. Data 14, 4251–4270. https://doi.org/10.5194/essd-14-4251-2022.

Hou, Y.Z., Xing, Q.G., Zheng, X.Y., Sheng, D.Z., Wang, F.T., 2023. Monitoring suspended sediment concentration in the Yellow River estuary and its vicinity waters on the basis of SDGSAT-1 multispectral imager. Water 15, 3522. https://doi.org/10.3390/w15193522.

Huang, J.H., Sun, W.T., Li, C., Lu, D., Wang, N.N., Wang, Q.Q., 2021. Analysis and evaluation of offshore wind energy resources characteristics based on WRF model. Acta Energ. Solaris Sin. 42, 278–283. https://doi.org/10.19912/j.0254-0096.tynxb.2017-1077.

ICF, 2021. Comparison of environmental effects from different offshore wind turbine foundations. In: U.S. Dept. of the Interior, Bureau of Ocean Energy Management, Headquarters, Sterling, VA. OCS Study BOEM 2021-053. 48 pp.

IEA (International Energy Agency), 2024. Renewables 2023: Analysis and Forecasts to 2028. https://www.iea.org/reports/renewables-2023 (accessed 12 December 2024).

Jiang, Y.Y., 2016. Jiemian New, China Successfully Grid-connects the Largest Single Offshore Wind Farm Ever Built. https://www.jiemian.com/article/910982.html (accessed 28 March 2024).

Jiang, B., 2022. China Energy Network, Bohai Bay Is Fertile Ground for Wind Power Development, With Top Companies Racing to Land. https://www.hxny.com/nd-78493-0-8.html (accessed 28 March 2024).

Jiang, B., Liu, H.L., Xing, Q.G., Cai, J.N., Zheng, X.Y., Li, L., Liu, S.S., Zheng, Z.M., Xu, H. Y., Meng, L., 2021. Evaluating traditional empirical models and BPNN models in monitoring the concentrations of Chlorophyll-A and total suspended particulate of eutrophic and turbid waters. Water 13, 650. https://doi.org/10.3390/w13050650.

Jiang, H., Yao, L., Zhou, C.H., 2023. Assessment of offshore wind-solar energy potentials and spatial layout optimization in mainland China. Ocean Eng. 287, 115914. https://doi.org/10.1016/j.oceaneng.2023.115914.

Keesing, J.K., Liu, D.Y., Fearns, P., Garcia, R., 2011. Inter-and intra-annual patterns of Ulva prolifera green tides in the Yellow Sea during 2007–2009, their origin and relationship to the expansion of coastal seaweed aquaculture in China. Mar. Pollut. Bull. 62, 1169–1182. https://doi.org/10.1016/j.marpolbul.2011.03.040.

Kuang, C.P., Qian, C.R., Yao, K.H., Gu, J., 2014. Responses of tidal current and sediment transport to Huanghua port. J. Tongji Univ. (Nat. Sci.) 42, 1516–1522. https://doi.org/10.11908/j.issn.0253-374x.2014.10.009.

Langhamer, O., Dahlgren, T.G., Rosenqvist, G., 2018. Effect of an offshore wind farm on the viviparous eelpout: biometrics, brood development and population studies in Lillgrund, Sweden. Ecol. Indic. 84, 1–6. https://doi.org/10.1016/j.ecolind.2017.08.035.

Lecordier, E.M., Gernez, P., Mazik, K., York, K., Forster, R.M., 2025. Quantification of turbid wakes in offshore wind farms using satellite remote sensing. Sci. Total Environ. 967, 178814. https://doi.org/10.1016/j.scitotenv.2025.178814.
Li, S.H., Tang, J.W., Yun, C.X., 2002. A study on the quantitative remote sensing model for the sediment concentration in estuary. Haiyang Xuebao 24, 51–58.
Li, X.M., Chi, L.Q., Chen, X.E., Ren, Y.Z., Lehner, S., 2014. SAR observation and numerical modeling of tidal current wakes at the East China Sea offshore wind farm. J. Geophys. Res-Oceans 119, 4958–4971. https://doi.org/10.1002/2014JC009822.
Li, X.Y., Fan, K., Chen, P.F., 2021. Three Gorges Energy, "Three Gorges Leading Vessel": China's floating offshore wind power, I am the "Wall Breaker". https://www.in-en.com/article/html/energy-2306723.shtml (accessed 12 December 2024).
Li, Z.C., Hu, P., Ma, J.X., Gao, M., Huang, H.L., Liu, X.Y., Qi, L., Sun, Z.H., 2022. Analysis and prospect of offshore wind power development in China. China Offsh. Oil Gas 34, 229–236.
Liu, Y., 2024. Zhiyan Consulting, Analysis of China's offshore wind turbine industry chain, development status, and competitive landscape in 2024: rapid growth driven by technological advancements and cost reductions, with policies and markets shaping the future. https://www.chyxx.com/industry/1201384.html (accessed 5 March 2024).
Liu, F.F., Zhang, T.H., Ye, H.B., Tang, S.L., 2021. Using satellite remote sensing to study the effect of sand excavation on the suspended sediment in the Hong Kong-Zhuhai-Macau bridge region. Water 13, 435. https://doi.org/10.3390/w13040435.
Liu, J.C., Liu, J.Q., Ding, J., Lu, Y.C., 2022. A refined imagery algorithm to extract green tide in the Yellow Sea from HY-1C satellite CZI measurements. Haiyang Xuebao 44, 1–11.
Ma, R.H., Tang, J.W., Duan, H.T., Pan, D.L., 2009. Progress in lake water color remote sensing. J. Lake Sci. 21, 143–158. https://doi.org/10.18307/2009.0201.
Maxwell, S.M., Kershaw, F., Locke, C.C., Conners, M.G., Dawson, C., Aylesworth, S., Loomis, R., Johnson, A.F., 2022. Potential impacts of floating wind turbine technology for marine species and habitats. J. Environ. Manag. 307, 114577. https://doi.org/10.1016/j.jenvman.2022.114577.
Mendel, B., Schwemmer, P., Peschko, V., Müller, S., Schwemmer, H., Mercker, M., Garthe, S., 2019. Operational offshore wind farms and associated ship traffic cause profound changes in distribution patterns of Loons (Gavia spp.). J. Environ. Manag. 231, 429–438. https://doi.org/10.1016/j.jenvman.2018.10.053.
Meng, R.L., Xing, Q.G., 2013. Detection of offshore ship and well platform based on optical remote sensing images. J. Comput. Appl. 33, 708–711.
National Energy Administration, 2025. Grid operation of renewable energy in 2024. https://www.nea.gov.cn/20250221/e10f363cabe3458aaf78ba4558970054/c.html (accessed 5 March 2025).
ORE(Offshore Renewable Energy) Catapult, ARUP, 2024. Floating Offshore Wind Anchor Review. PN000585-RPT-005-Rev.01.
Ou, J.T., Dong, H.Y., Jia, L.W., Luo, X.X., He, Z.X., Chen, K.L., Liu, J., Lin, Y.T., Yu, M.D., Liang, M.G., 2022. Short-term variations and influencing factors of suspended sediment concentrations at the Heisha Beach, Guangdong, China. Acta Oceanol. Sin. 41, 51–63. https://doi.org/10.1007/s13131-021-1874-3.
Pahlevan, N., Mangin, A., Balasubramanian, S.V., et al., 2021. ACIX-Aqua: a global assessment of atmospheric correction methods for Landsat-8 and Sentinel-2 over lakes, rivers, and coastal waters. Remote Sens. Environ. 258, 112366. https://doi.org/10.1016/j.rse.2021.112366.
Qin, H.Y., 2022. Review and prospect of offshore wind power development in China. Mar. Econ. 12, 50–58. https://doi.org/10.19426/j.cnki.cn12-1424/p.2022.02.003.
Spiga, I., Aldred, N., Caldwell, G.S., 2017. Anthropogenic noise compromises the anti-predator behaviour of the European seabass, Dicentrarchus labrax (L.). Mar. Pollut. Bull. 122, 297–305. https://doi.org/10.1016/j.marpolbul.2017.06.067.
Su, W., Wu, N., Zhang, L.L., Chen, M.R., 2020. A review of research on the effect of offshore wind power project on marine organisms. Mar. Sci. Bull. 39, 291–299. https://doi.org/10.11840/j.issn.1001-6392.2020.03.002.
Vanermen, N., Onkelinx, T., Verschelde, P., Courtens, W., Van de walle, M., Verstraete, H., Stienen, E.W.M., 2015. Assessing seabird displacement at offshore wind farms: power ranges of a monitoring and data handling protocol. Hydrobiologia 756, 155–167. https://doi.org/10.1007/s10750-014-2156-2.
Vanhellemont, Q., Ruddick, K., 2014. Turbid wakes associated with offshore wind turbines observed with Landsat 8. Remote Sens. Environ. 145, 105–115. https://doi.org/10.1016/j.rse.2014.01.009.
Wang, Y., Yang, H., Zhang, W., 2021. Simulation of sediment erosion and silting on Rudong offshore wind farm project in Jiangsu province by MIKE21. Trans. Oceanol. Limnol. 43, 48–57. https://doi.org/10.13984/j.cnki.cn37-1141.2021.02.007.
Wang, T., Yu, X.S., Zhang, L.B., 2022. Research progress on the comprehensive impact of offshore wind farms on the marine ecological environment and biological resources. Mar. Sci. 46, 95–104. https://doi.org/10.11759/hykx20211115001.
Wang, X., Lin, P., Huang, H.D., Yuan, J., Qiu, X., Liu, X., 2023. Scour dynamic properties and online monitoring of offshore wind power foundation. J. Tsinghua Univ. (Sci. Technol.) 63, 1087–1094. https://doi.org/10.16511/j.cnki.qhdxxb.2023.26.007.
Wang, K.C., Xiao, W., He, T.T., Zhang, M.X., 2024. Remote sensing unveils the explosive growth of global offshore wind turbines. Renew. Sust. Energ. Rev. 191, 114186. https://doi.org/10.1016/j.rser.2023.114186.
Wong, B.A., Thomas, C., Halpin, P., 2019. Automating offshore infrastructure extractions using synthetic aperture radar & Google Earth Engine. Remote Sens. Environ. 233, 111412. https://doi.org/10.1016/j.rse.2019.111412.
Xie, J.B., Feng, X.R., Gao, T.H., Wang, Z.F., Wan, K., Yin, B.S., 2024. Application of deep learning in predicting suspended sediment concentration: a case study in Jiaozhou Bay, China. Mar. Pollut. Bull. 201, 116255. https://doi.org/10.1016/j.marpolbul.2024.116255.
Xing, Q.G., Lou, M.J., Chen, C.Q., Shi, P., 2013. Using in situ and satellite hyperspectral data to estimate the surface suspended sediments concentrations in the Pearl River estuary. IEEE J-STARS 6, 731–738. https://doi.org/10.1109/JSTARS.2013.2238659.
Xing, Q.G., Lou, M.J., Tian, L.Q., Yu, D.F., Braga, F., Tosi, L., Wu, L.L., 2014. Quasi-simultaneous measurements of suspended sediments concentration (SSC) of very turbid waters at the Yellow River estuary with the multi-spectral HJ-1 imageries and in-situ sampling. In: Paper presented at the Conference on Ocean Remote Sensing and Monitoring From Space, Beijing, Peoples R China. https://doi.org/10.1117/12.2068930.
Xu, L., Li, F., Peng, H.B., 2015. Development of offshore wind power and its environmental problems in China. China Popul. Resour. Environ. 25, 135–138.
Xu, W.X., Liu, Y.X., Wu, W., Dong, Y.Z., Lu, W.Y., Liu, Y.C., Zhao, B.X., Li, H.T., Yang, R. F., 2020. Proliferation of offshore wind farms in the North Sea and surrounding waters revealed by satellite image time series. Renew. Sust. Energ. Rev. 133, 110167. https://doi.org/10.1016/j.rser.2020.110167.
Yang, Q.Q., Jin, C.Y., Li, T.W., Yuan, Q.Q., Shen, H.F., Zhang, L.P., 2022. Research progress and challenges of data driven quantitative remote sensing. Natl. Remot. Sens. Bull. 26, 268–285. https://doi.org/10.11834/jrs.20211410.
Yu, S., 2024. Zhiyan Consulting, Analysis of the current status and trends of floating offshore wind power development globally and in China in 2024. https://www.chyxx.com/industry/1184672.html (accessed 12 December 2024).
Yu, W.C., Zhang, Z.L., 2017. Recognition of tide and tidal current movement in the Yangtze estuary. J. Water Resour. Res. 6, 475–485. https://doi.org/10.12677/JWRR.2017.65056.
Yu, Z.F., Chen, X.L., Tian, L.Q., Zhou, B., 2012. Atmospheric correction method for Poyang lake HJ-1A /B CCD image. Geomat. Inform. Sci. Wuhan Univ. 37, 1078–1082. https://doi.org/10.13203/j.whugis2012.09.004.
Zhang, J.H., Wang, H., 2022. Development of offshore wind power and foundation technology for offshore wind turbines in China. Ocean Eng. 266, 113256. https://doi.org/10.1016/j.oceaneng.2022.113256.
Zhang, T., Tian, B., Sengupta, D., Zhang, L., Si, Y.L., 2021. Global offshore wind turbine dataset. Sci. Data 8, 191. https://doi.org/10.1038/s41597-021-00982-z.
Zhang, F.F., Li, J.S., Wang, C., Wang, S.L., Wang, Z., Zhang, B., 2023. Multitype inland water atmospheric correction and water quality estimation based on HY-1C CZI images. Natl. Remot. Sens. Bull. 27, 79–91. https://doi.org/10.11834/jrs.20235010.
Zhao, B., Zhou, Y.R., Xing, C.C., Liu, N.N., Li, J., Kang, J.L., 2022. Study on the impact of Tangshan laoting bodhi island offshore windfarms on marine ecological space. Mar. Environ. Sci. 41, 496–503. https://doi.org/10.13634/j.cnki.mes.2022.04.009.
Zheng, C.W., Li, C.Y., 2023. Research on offshore wind energy classification: Bottlenecks and countermeasures. Bull. Chin. Acad. Sci. 38, 654–665. https://doi.org/10.16418/j.issn.1000-3045.20220605002.
Zhou, D.K., Xu, J.H., Chen, D.D., Wu, X.Q., Liu, S.S., Zhao, X., 2023. Research and practice on marine environmental impact tracking evaluation index system of offshore wind power projects during construction. Ocean Dev. Manag. 40, 59–66. https://doi.org/10.20016/j.cnki.hykfygl.20231220.006.